

Experimental Investigation on the Effect of Crescent Planform on Lift and Drag

C. P. van Dam*

University of California, Davis, Davis, California 95616

P. M. H. W. Vijgen†

High Technology Corporation, Hampton, Virginia 23666

and

B. J. Holmes‡

NASA Langley Research Center, Hampton, Virginia 23665

Lift and drag forces were compared for elliptic and crescent wing models at cruise and climb conditions in the NASA Langley 14×22 ft subsonic tunnel. The force measurements were obtained for an angle-of-attack range from -3 to 10 deg at a Reynolds number (based on the freestream conditions and the average wing chord) of about 1.7×10^6 . The experiment and the accuracy of the measurements are discussed in detail. In addition, lift and drag measurements are summarized for high angle-of-attack conditions. The results indicate that, for attached flow conditions, the crescent wing with its highly swept tips generated less lift-dependent drag than the elliptic wing for given lift force, wing span, and freestream conditions. The drag reduction is thought to be the result of a favorable influence of trailing wake deformation on the pressure distribution of the crescent wing.

Introduction

THE purpose of the wind-tunnel experiment was to evaluate the effects of a planar planform modification on the lift-dependent drag of finite aspect ratio wings. Previously published theoretical nonlinear, inviscid results predict lower induced drag for a planar wing with highly swept tips than for an elliptic wing for given lift, span, and freestream conditions (e.g., Refs. 1 and 2). The reduction in drag is thought to be the result of a favorable influence of trailing wake deformation and roll-up on the pressure distribution of wings with highly swept tips. These nonplanar wake effects are neglected in the classical wing theory (e.g., Refs. 3 and 4).

The crescent wing has a continuously swept planform with zero sweep at the wing root and 90-deg sweep at the tip. Otherwise, it is completely identical to the elliptic wing. Thus, the elliptic and the crescent wing have identical span and spanwise chord distribution (and, consequently, identical area and aspect ratio). As a result of the sweep, the spanwise load distributions of the two wings differ slightly. However, the crescent wing performs better than the elliptic wing, according to inviscid induced-drag calculations.

A low-speed wind-tunnel experiment was conducted to determine whether the predicted induced-drag benefits could be realized when viscous effects are included. Potentially, the three-dimensional boundary-layer behavior on highly swept surfaces increases viscous drag and, thus, could mask any inviscid performance benefits due to the crescent shape. This paper presents the experimental setup, accuracy, and results for an elliptic and a crescent wing planform of aspect ratio 7.

Drag Analysis

The familiar expression for the drag coefficient C_D of an untwisted wing with a symmetrical section shape at subsonic conditions is

$$C_D = C_{D,0} + \frac{C_L^2}{\pi ARe} \quad (1)$$

where $C_{D,0}$ represents the zero-lift drag coefficient, C_L is the lift coefficient, AR the aspect ratio of the wing, and e the Oswald efficiency factor. The second term on the right side of Eq. (1) represents the lift-dependent drag coefficient $C_{D,L}$. Best cruise efficiency is obtained when the drag is minimized for a given lift at $C_L = \sqrt{C_{D,0} \pi ARe}$. In this case, the lift-dependent drag contributes 50% of the total drag, and it becomes clear that a reduction in this drag term contributes significantly to an improvement in airplane efficiency. The lift-dependent drag coefficient can also be written in the following form:

$$C_{D,L} = \frac{C_L^2}{\pi ARe} = \left(K_p + \frac{K_i}{\pi AR} \right) C_L^2 \quad (2)$$

where K_p represents the profile-drag factor and K_i represents the induced-drag factor. The term $K_i C_L^2 / (\pi AR)$ is called the induced-drag coefficient $C_{D,i}$, and for $K_i = 1.0$, it represents the minimum induced-drag coefficient from classical theory for a planar wing with an elliptic spanwise load distribution.

For subsonic inviscid calculations, $C_{D,0} = K_p = 0$ and K_i can be determined from the slope of the linearized drag polar, $C_D = C_{D,i}$ vs C_L^2 . However, for viscous-flow calculations and experiments, the slope of the linearized drag polar is not only dependent on K_i and AR but also on the value of K_p . The individual contributions of K_p and K_i cannot be determined easily. In Ref. 5, this problem was overcome by using a laminar section shape for the wing. Inside the low-drag region of the drag polar (the so-called drag bucket) $K_p \approx 0$ and, thus, K_i can be calculated from the slope of the linearized drag polar for the appropriate angle-of-attack range. In the present experiment, the centerbody and the center wing panel (see Figs. 1) were obtained from an existing wind-tunnel model.⁶ This dictated the turbulent NACA 0012 section shape for both wing configurations. Therefore, in this paper the comparison of the performance of the various configurations will be based on the

Received April 9, 1990; revision received Nov. 28, 1990; accepted for publication Dec. 20, 1990. This paper is declared a work of the U.S. Government and is not subject to copyright protection in the United States.

*Associate Professor, Department of Mechanical, Aeronautical, and Materials Engineering. Member AIAA.

†Research Scientist. Member AIAA.

‡Deputy Director for Aeronautics (Acting). Associate Fellow AIAA.

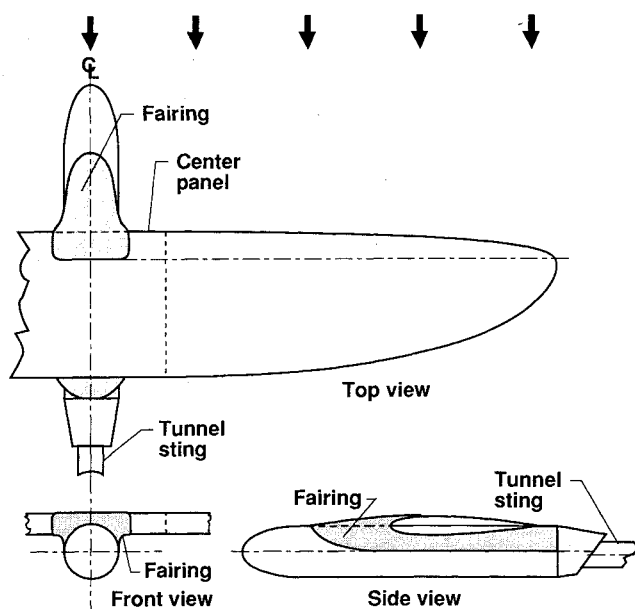


Fig. 1 Geometry of elliptic and crescent wind-tunnel models.

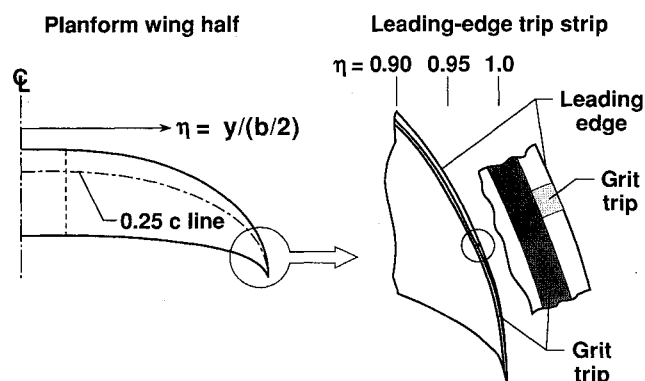
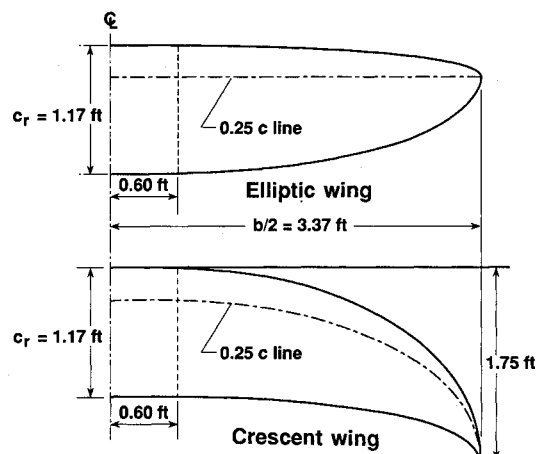


Fig. 2 Leading-edge boundary-layer transition trip on crescent wing.

value of the Oswald efficiency factor e . Future numerical and physical experiments will concentrate on separating the viscous and the induced-drag contributions to the lift-dependent drag.

Experiment

The effects of a crescent planform shape on the lift and drag characteristics were investigated by direct comparison with an elliptical planform. The test conditions and two wing configurations were identical to those described in Ref. 7. The elliptic wing had a straight and unswept quarter chord, whereas the quarter chord of the crescent wing was curved backward (Figs. 1). Otherwise, the two configurations were exactly the same. Both had identical wing areas ($S = 6.47 \text{ ft}^2$), wing span ($b = 6.74 \text{ ft}$), aspect ratio ($AR = 7.014$), spanwise chord distribution (constant for the center panel and elliptic for the outboard panel), and section shape in the freestream direction (NACA 0012). Also, both models had zero wing twist and zero dihedral. The dynamic pressure, the unit Reynolds number, and the Mach number of the freestream during the test in the $14 \times 22 \text{ ft}$ subsonic tunnel at the NASA Langley Research Center were approximately 100 lb/ft^2 , $1.8 \times 10^6/\text{ft}$ and 0.27 , respectively. For a reference wing chord of 0.96 ft , this translated into a test Reynolds number of about 1.7×10^6 . Note that, in the experiment reported in Ref. 6, the center panel of the wing is mounted on top of the cylindrical centerbody without any fairing. This wing-body combination tends to result in adverse aerodynamic interference between the wing

and the body.⁸ In the present experiment (as well as the high- α experiment⁷), the adverse interference was eliminated by adding a suitable fillet (see Figs. 1). This fillet eliminated breakdown of the flow on top of the body ahead of the wing (as confirmed by flow visualizations) and improved the flow in the wing-body juncture by widening the angle between the side of the body and the lower surface of the wing.

In order to obtain the results reported in Ref. 7 (and partly summarized in this paper), the models were mounted on a six-component internal strain-gauge balance providing axial-, side-, and normal-force as well as rolling-, pitching-, and yawing-moment measurements. The six-component balance was sized to allow high- α measurements at the test conditions. The objective of the experiment reported in this paper was to measure accurately the lift and the drag force for attached flow conditions (i.e., cruise/climb conditions). Consequently, the models were mounted on a more sensitive three-component strain-gauge balance providing axial-force, normal-force, and pitching-moment measurements. The maximum load for the present test conditions was reached at $\alpha = 10 \text{ deg}$ with this balance.

Boundary-layer transition was fixed on both models at 5% of the chord (in the freestream direction) over the upper and lower surfaces along the entire span. The trips consisted of densely distributed carborundum grit with a nominal roughness height of 0.008 in . The particle size was selected using the method of Ref. 9. The width of the trip strips was 0.125 in . Over the crescent-wing model, attachment-line trip strips were located around the leading edge at about $\eta = \pm 0.98$ (Fig. 2). These trips were oriented normal to the leading edge to ensure transition of the leading-edge attachment-line boundary layer along the highly swept tips.¹⁰ On the centerbody, the transition was fixed circumferentially at 3.0 in downstream of the nose. Flow visualizations confirmed transition of the boundary layer at the trips.

Both configurations were tested right side up (high wing) and upside down (low wing). To ensure invariant flow conditions, both models were tested at the centerline of the tunnel-test section and data were taken at 0.5-deg increments for an angle of attack ranging from -3 to 10 deg . Around $\alpha = 0 \text{ deg}$, 0.25-deg increments in angle of attack were taken in order to determine the zero-lift angle accurately.

Windoff tares were carefully determined for each configuration. The analog data signals were low-pass filtered (7.5 Hz) to remove the effects of model and tunnel vibrations and dynamic-pressure fluctuations. At each angle of attack, bal-

ance readings were taken over a period of 20 s at a rate of 5 data sampling cycles/s. In the figures, each datum point represents the average value of these readings. The uncertainties in the measurement of the lift and drag coefficients for the data points are based on the accuracies of the internal balance, the angle-of-attack measurement, and the dynamic-pressure transducer. The balance was calibrated using the actual loading combinations encountered in this experiment and the maximum errors were $\pm 0.26\%$ of full axial load (100 lb) and $\pm 0.13\%$ of full normal load (600 lb). The dynamic pressure had an accuracy of $\pm 0.04\%$ of full scale (209 lb/ft²). The angle of attack was determined with an electronic inclinometer mounted in the nose cone of the centerbody. The uncertainty in the angle-of-attack measurement was determined to be ± 0.025 deg. An error analysis indicates the following maximum errors in the lift coefficient C_L and the drag coefficient C_D for $\alpha = 0$ deg (see the Appendix): $\Delta C_L = \pm 0.001$, $\Delta C_D = \pm 0.0004$. For $\alpha = 10$ deg, $\Delta C_L = \pm 0.002$, $\Delta C_D = \pm 0.0012$.

In Figs. 3, the normal force F_N and the axial force F_A are presented at zero-wind conditions. These plots provide an example of the accuracy of the force measurements obtained in the experiment. The forces should be zero at these conditions. Small deviations from zero were measured for both force components. However, these deviations fall within the error band of the measuring system. Another indicator of the quality of the experiment is the repeatability of the lift and drag results. In Figs. 4, three separate sets of data for the crescent-wing model are presented for the pertinent α range. A comparison of the data shows the following repeatability: $\Delta C_L = \pm 0.001$, $\Delta C_D = \pm 0.0003$. This repeatability is better than the previously discussed error band of the three-component balance.

The wind tunnel had a slightly expanding test section; therefore, the buoyancy correction¹¹ for the models was negligible and omitted. The solid-blockage and wake-blockage effects on

the dynamic pressure¹¹ were very small (and identical for both models) as a result of the small size of the wing-body model (maximum cross-sectional area of 0.93 ft²) relative to the cross-sectional area of the test section (315.4 ft² at the inlet and 318.7 ft² at the outlet). The only significant correction was due to the walls of the closed-throat wind tunnel. The calculated downwash correction (including the wake-deflection effect) is $\Delta\alpha_{\text{wall}} = 0.154C_L$ deg for the crescent wing and $\Delta\alpha_{\text{wall}} = 0.156C_L$ deg for the elliptic wing. These predictions are obtained with the surface-panel method of Ref. 12. These wall corrections are not applied to the geometric angle-of-attack readings to prevent contamination of the experimental data with approximate corrections. The effect of the wall correction on the measured lift-dependent drag will be estimated in the discussion of the data.

The geometric angle-of-attack readings were corrected for the measured flow angularity in the test section at the given test conditions. An average flow angularity of $\Delta\alpha_{\text{flow}} = 0.075$ deg (upflow) for both the elliptic- and the crescent-wing model was measured at the centerline of the test section by comparing the normal-force data for the model right side up and the model upside down.

Results

In Fig. 5, the lift curves are presented for both wings in the right-side-up position. The lift and drag coefficients were nondimensionalized by the reference area of 6.47 ft² and the freestream dynamic pressure. The lift curves for both wings were very similar; for $C_L > 0.5$, both curves became nonlinear under the influence of the viscous effects. Using the method of least squares, a linear polynomial can be fitted to the data for $0 < C_L < 0.5$. The calculated lift-curve slope for the elliptic wing is $C_{L,\alpha} = 0.0792$ deg⁻¹ and for the crescent wing $C_{L,\alpha} = 0.0789$ deg⁻¹.

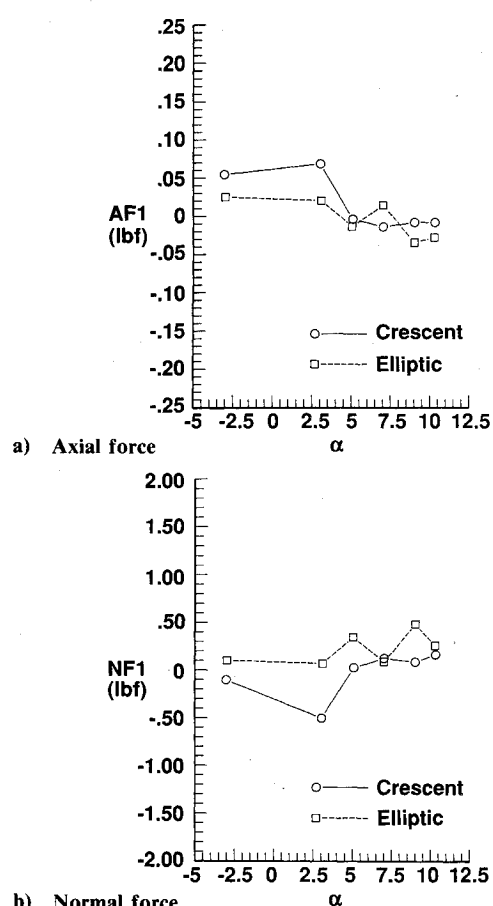


Fig. 3 Zero-wind force measurements.

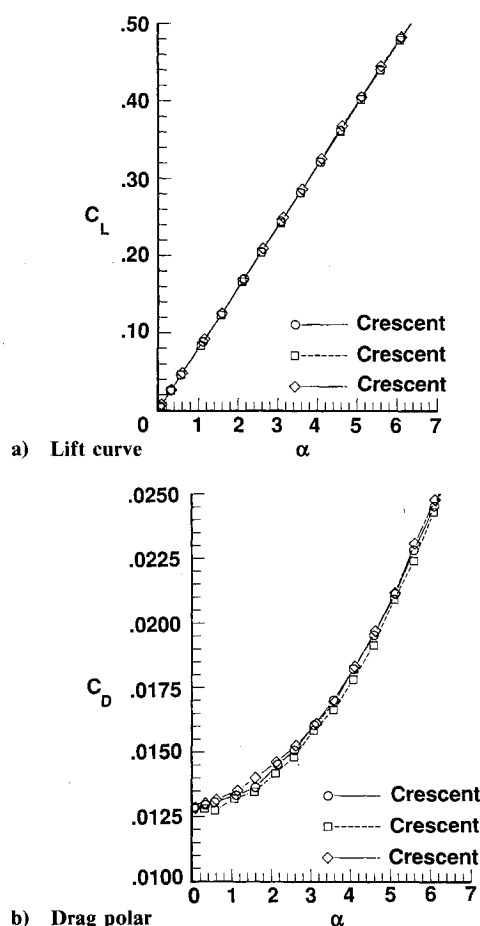


Fig. 4 Comparison of results for three separate data runs (crescent model).

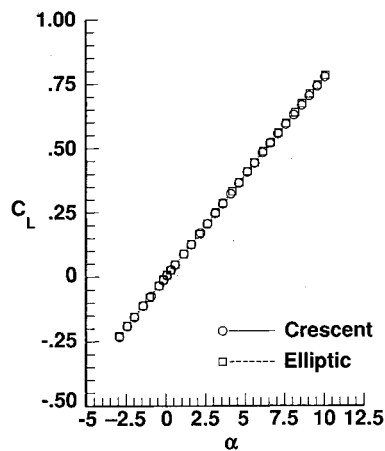
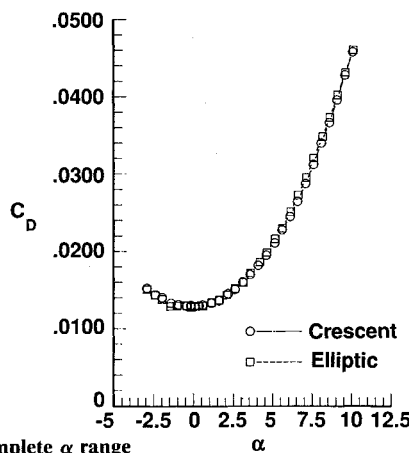
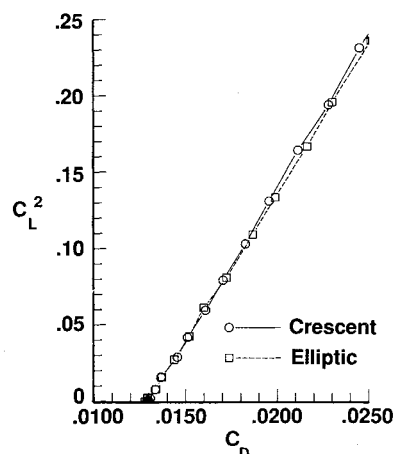


Fig. 5 Lift curves of elliptic and crescent configuration (models right side up).



a) Complete α range



b) Linearized drag polar for $0 < C_L < 0.5$

Fig. 6 Drag data of elliptic and crescent configuration (models right side up).

In Figs. 6, the drag polars are presented for both wings in the right-side-up position. The results show that the crescent wing produced less lift-dependent drag than the elliptic wing for most of the α range. For both wings, a change in the slope of the curve was measured for $C_L > 0.5$. Equation (1) can be fitted to the data for $0 < C_L < 0.5$. For the elliptic wing, the resulting expression is

$$C_D = C_{D,0} + \frac{C_L^2}{\pi AR e} = 0.0129 + \frac{C_L^2}{\pi AR (0.875)} \quad (3a)$$

and for the crescent wing,

$$C_D = 0.0130 + \frac{C_L^2}{\pi AR (0.903)} \quad (3b)$$

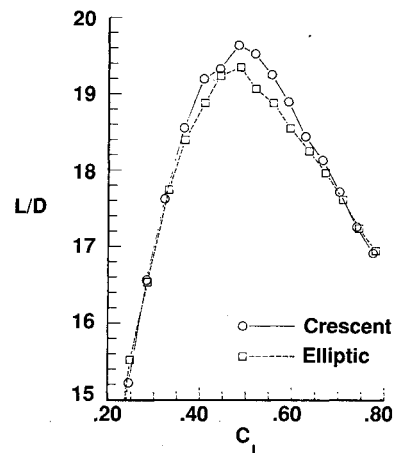


Fig. 7 L/D curves of elliptic and crescent configuration (models right side up).

where the aspect ratio $AR = 7.014$. Thus, the Oswald efficiency factor e improved by 3.2% as a result of the crescent planform shape. The difference in the values for $C_{D,0}$ is within the previously discussed error band.

For a parabolic drag polar, the maximum lift-to-drag ratio is

$$\left(\frac{L}{D}\right)_{\max} = 0.5 \sqrt{\frac{\pi AR e}{C_{D,0}}} \quad (4)$$

or $(L/D)_{\max} = 19.57$ (based on $C_{D,0} = 0.0130$ and $e = 0.903$) for the crescent wing and $(L/D)_{\max} = 19.33$ ($C_{D,0} = 0.0129$ and $e = 0.875$) for the elliptic wing. In Fig. 7, the measured L/D values are plotted as function of C_L . The measured maximum lift-to-drag ratio for the crescent wing was $(L/D)_{\max} = 19.63$, whereas for the elliptic wing the measured $(L/D)_{\max} = 19.35$. Thus, good agreement is shown between the calculated values of $(L/D)_{\max}$ and the measured values of $(L/D)_{\max}$.

In Figs. 8 and 9, flow visualizations are presented for the elliptic and the crescent model in the right-side-up position. The surface-flow patterns in the form of titanium-dioxide streak lines demonstrate that the streamwise patterns were very symmetric with respect to the longitudinal axis of the model for both wing configurations. The streak lines ran nearly parallel to the longitudinal axis of the elliptic configuration at both $\alpha = 0$ and 7 deg. No flow separation was detectable in the oil-flow patterns at these angles of attack. The flow patterns for the crescent configuration were also very symmetric at both angles depicted. However, in the wingtip regions, the streak lines displayed a strong outward curvature at $\alpha = 7$ deg, indicating significant three-dimensional viscous-flow effects.

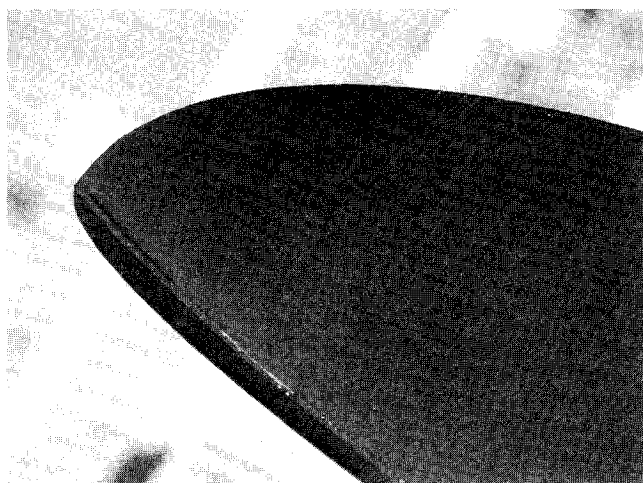
In Figs. 10–12, the lift and drag results for both wings in the upside-down position are presented. For $0 < C_L < 0.5$, the lift-curve slope of the elliptic wing is determined to be $C_{L,\alpha} = 0.0791 \text{ deg}^{-1}$, whereas for the crescent wing, $C_{L,\alpha} = 0.0789 \text{ deg}^{-1}$. These values are virtually identical to those measured for the models in the right-side-up position. In Fig. 12, the drag data are presented. For $0 < C_L < 0.5$, the least-squares fit for the elliptic wing gives

$$C_D = 0.0129 + \frac{C_L^2}{\pi AR (0.911)} \quad (5a)$$

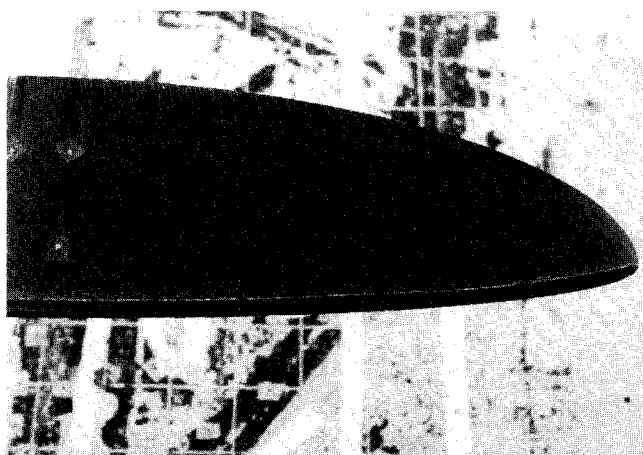
and for the crescent wing,

$$C_D = 0.0128 + \frac{C_L^2}{\pi AR (0.924)} \quad (5b)$$

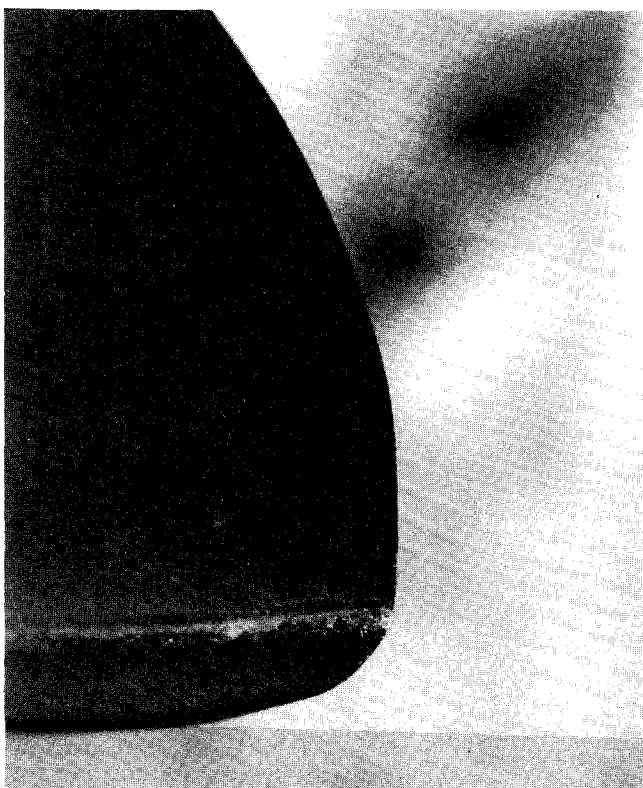
The values for the Oswald efficiency factor are slightly higher than those measured for the models in the right-side-up posi-



a) Right wingtip, $\alpha = 0$ deg

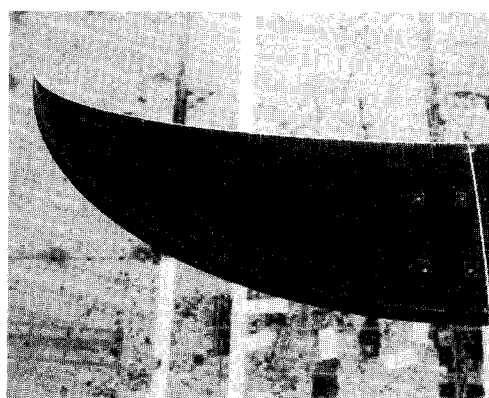


b) Left wing, $\alpha = 7$ deg

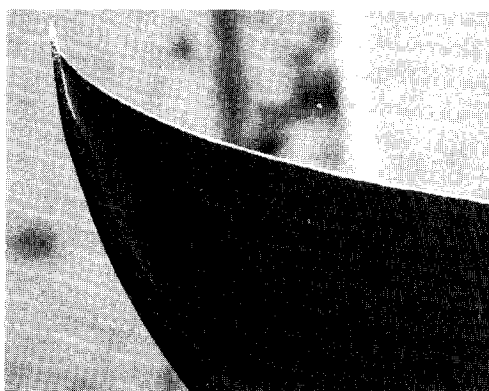


c) Left wingtip, $\alpha = 7$ deg

Fig. 8 Titanium-dioxide streak-line patterns over elliptic wing (freestream direction from bottom to top).



a) Right wing, $\alpha = 0$ deg



b) Right wingtip, $\alpha = 0$ deg



c) Right wing, $\alpha = 7$ deg



d) Right wingtip, $\alpha = 7$ deg

Fig. 9 Titanium-dioxide streak-line patterns over crescent wing (freestream direction from bottom to top).

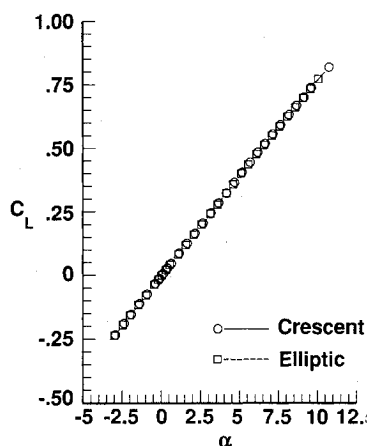


Fig. 10 Lift curves of elliptic and crescent configuration (models upside down).

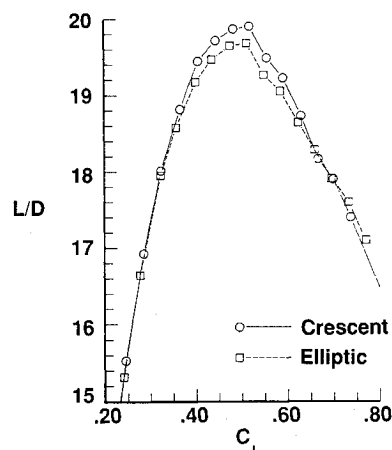
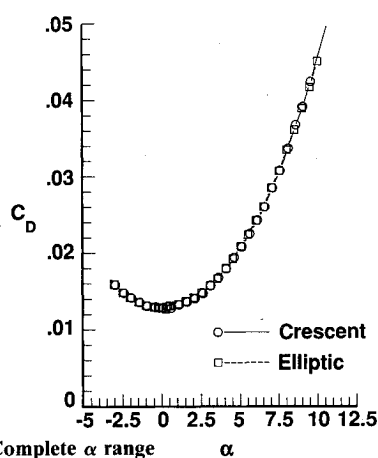
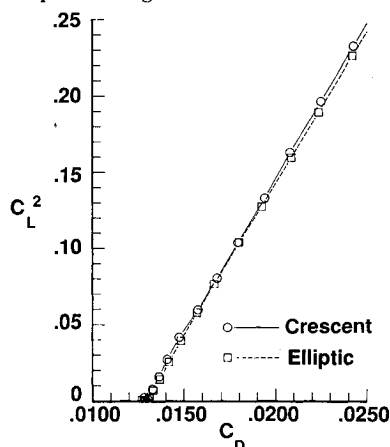


Fig. 12 L/D curves of elliptic and crescent configuration (models upside down).



a) Complete α range



b) Linearized drag polar for $0 < C_L < 0.5$

Fig. 11 Drag data of elliptic and crescent configuration (models upside down).

tion. This improvement in the performance is also reflected in the L/D curves shown in Fig. 12. For the elliptic wing, the measured value for $(L/D)_{\max}$ was 19.68 and the calculated value (based on $C_{D,0} = 0.0129$ and $e = 0.911$) is 19.72. For the crescent wing, the measured value was $(L/D)_{\max} = 19.90$ and the calculated value is $(L/D)_{\max} = 19.94$ ($C_{D,0} = 0.0128$ and $e = 0.924$).

In Ref. 7, the high-angle-of-attack aerodynamic characteristics of the crescent and the elliptic configuration are discussed. In Fig. 13, the lift characteristics are repeated for completeness, whereas the drag polars for the two configurations are presented in Fig. 14. Note that these results were obtained with the less accurate six-component balance. The balance was

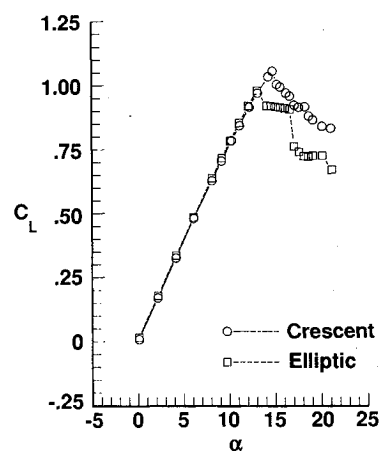


Fig. 13 Lift curves of elliptic and crescent configuration (models right side up, 6-component balance).

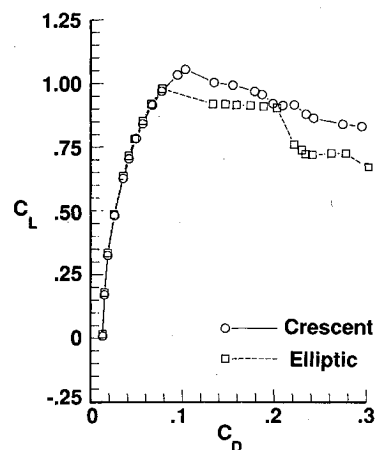


Fig. 14 Drag polars of elliptic and crescent configuration (models right side up, 6-component balance).

sized to handle the static and the dynamic loads at stall and poststall test conditions. In Fig. 13, the enhanced lift capabilities due to the crescent shape at stall angles are clearly noticeable. Flow-visualization studies indicate that this increment in lift is the result of leading-edge, separation-induced vortex flow over the highly swept tip regions of the crescent wing.⁷ The drag characteristics of the two wings at high angles of attack were similar (Fig. 14). At $\alpha = 13$ deg, the elliptic wing reached its maximum lift capabilities and the drag increased very rapidly for angles of attack beyond stall. For the crescent wing the drag rise occurred at the stall angle $\alpha = 14.5$ deg. Note that at high (pre-stall) angles of attack ($\alpha > 10$ deg) the

crescent model produced slightly more drag at given lift coefficient than the elliptic model. This increment in drag is consistent with the highly three-dimensional flow and the limited trailing-edge separation observed over the outboard portion of the crescent wing at these conditions.⁷

Discussion

The wind-tunnel results in the previous section illustrate the performance characteristics of the elliptic and the crescent model in terms of the lift-curve slope $C_{L,\alpha}$ and the Oswald efficiency factor e at Mach number $M_\infty = 0.27$ and Reynolds number $Re = 1.7 \times 10^6$. In this section, these results are examined in more detail.

Induced-drag calculations are generally conducted using inviscid methods. The resulting value for the induced-drag factor K_i cannot be compared directly with the experimentally determined value for e , as explained previously. For the elliptic model in the upside-down position, $e = 0.911$ for the lift range $0 < C_L < 0.5$, whereas the e value for the model right side up is slightly lower. Equation (2) shows that e is a function of both K_i and K_p for a given AR . An analysis of the profile-drag contribution to the lift-dependent drag using an airfoil analysis method¹³ and strip theory indicates $K_p \approx 0.00279$ for the elliptic wing and the pertinent C_L range. (Because of the three-dimensional boundary-layer effects, this calculation method is not suitable for the crescent wing.) Now, the induced-drag factor K_i can be determined. However, beforehand, we must examine the previously omitted wind-tunnel wall correction. The wall correction for the elliptic wing is calculated to be $\Delta\alpha_{wall} = 0.156 C_L$ deg. The corresponding lift-dependent drag correction $\Delta C_{D,L} \approx C_L^2 \Delta\alpha_{wall} = 0.00272 C_L^2$.¹¹ Thus, the wall correction and the profile-drag contribution appear to cancel each other and, consequently, $K_i \approx 1/e = 1.098$ for the elliptic wing in the upside-down position.

The effect of compressibility on the induced drag characteristics is often overlooked. According to the Prandtl-Glauert-Göthert transformation, the following scaling formulas can be derived to correlate compressible and incompressible ($M_\infty = 0$) results:

$$C_{D,i} = (C_{D,i})_{M=0}/\beta \quad (6a)$$

$$C_L = (C_L)_{M=0}/\beta \quad (6b)$$

$$AR = (AR)_{M=0}/\beta \quad (6c)$$

where $\beta = (1 - M_\infty^2)^{0.5}$.¹⁴ Consequently, the formula for the induced-drag coefficient in relation to the lift coefficient re-

mains independent of M_∞ . However, for a constant reference aspect ratio $AR^* = (AR)_{M=0} = 7.014$, the induced-drag factor is affected by the transformation as follows:

$$(K_i)_{M=0} = \frac{(C_{D,i})_{M=0} \pi (AR)_{M=0}}{(C_L)_{M=0}^2} = \frac{C_{D,i} \pi AR^*}{\beta C_L^2} = \frac{K_i}{\beta} \quad (7)$$

The resulting induced-drag factor at incompressible conditions for the elliptic wing in the upside-down position is $(K_i)_{M=0} = 1.098/\beta = 1.140$ ($M_\infty = 0.27$). This experimentally determined value for K_i is 14% higher than the K_i value from classical incompressible linear theory. The cause of this discrepancy is currently not well understood. Future numerical and wind-tunnel experiments (including surface-pressure measurements) must further concentrate on separating the contributions of K_p and K_i to the lift-dependent drag.

For an unswept wing of $AR^* = 7.014$ with an elliptic spanwise loading at $M_\infty = 0.27$, the theoretical lift-curve slope is $C_{L,\alpha} = 0.0850 \text{ deg}^{-1}$.¹⁴ The slope for the elliptic wing, as obtained from the measurements, is $C_{L,\alpha} = 0.0791 \text{ deg}^{-1}$ for $0 < C_L < 0.5$ at the test conditions. Inclusion of the wall correction reduces this value to $C_{L,\alpha} = 0.0781 \text{ deg}^{-1}$. Thus, the experimentally determined value for the lift-curve slope of the elliptic wing is less than the theoretically obtained value. In part, this discrepancy can be attributed to viscous contributions. However, further study is required to explore such effects as that of the centerbody on the lift curve.

In Tables 1 and 2, the complete data sets are presented for the models in the right-side-up and the upside-down positions, respectively. The results indicate that the lift-curve slope and the zero-lift drag coefficient were hardly affected by the planform shape or the model orientation. Only the Oswald efficiency factor was significantly changed by both the shape of the planform and the orientation of the model. Although the differences in the values for e are small, the results indicate consistently that the crescent model was more efficient than the elliptic configuration in both the right-side-up and the upside-down position. The improvement in the Oswald efficiency factor was $\Delta e \approx 3.9\%$ for the models right side up and $\Delta e \approx 2.1\%$ for the models upside down.

Concluding Remarks

A low-subsonic wind-tunnel experiment was conducted to evaluate the effects of a planar planform modification on the lift-dependent drag characteristics of finite aspect ratio wings. Forces were measured and flow visualizations were conducted to compare the aerodynamic characteristics of an unswept elliptic-wing model and a crescent-wing model with highly swept tips. Both models were tested in the right-side-up and the upside-down position at low-to-moderate angles of attack. The wind-tunnel results showed that, in the range of lift coefficients $0 < C_L < 0.5$, 1) the lift curve and the linearized drag polar were virtually linear, 2) the flow was fully attached over both models, 3) the lift-curve slope was unaffected by both the planform shape as well as the model position, 4) the Oswald efficiency factor was improved by approximately 3.9% as a result of the crescent planform shape for the models in the right-side-up position, 5) this improvement in the Oswald efficiency factor was about 2.1% for the models upside down, and 6) both the elliptic and the crescent model generated less drag for given lift in the upside down position than in the right-side-up position. Additionally, at high (pre stall) angles of attack, the elliptic model produced slightly less drag for given lift than the crescent model.

A study of the test accuracies indicates that the measured changes in the performance are of the same order as the maximum measurement errors. The largest single contribution to the test inaccuracies comes from the error in the angle-of-attack measurement. In the present test, the angle-of-attack readings were corrected for an average upflow angle

Table 1 Summary of results (models right side up)

Configuration	$(L/D)_{\max}$ measured	$0 < C_L < 0.5$			$(L/D)_{\max}$ calculated
		$C_{L,\alpha}$, deg ⁻¹	$C_{D,0}$	e	
Elliptic	19.38	0.0793	0.0128	0.868	19.33
Elliptic	19.35	0.0792	0.0129	0.875	19.33
Crescent	19.63	0.0789	0.0130	0.903	19.57
Crescent	19.71	0.0789	0.0128	0.908	19.77
Crescent	19.47	0.0792	0.0130	0.906	19.57

Table 2 Summary of results (models upside down)

Configuration	$(L/D)_{\max}$ measured	$0 < C_L < 0.5$			$(L/D)_{\max}$ calculated
		$C_{L,\alpha}$, deg ⁻¹	$C_{D,0}$	e	
Elliptic	19.46	0.0788	0.0131	0.890	19.34
Elliptic	19.68	0.0791	0.0129	0.911	19.72
Crescent	19.75	0.0790	0.0130	0.914	19.68
Crescent	19.90	0.0789	0.0128	0.924	19.94

$\Delta\alpha_{\text{flow}} = 0.075$ deg. The spanwise variation in the flow angularity is difficult to measure and was not known for the present test. This spanwise variation can greatly contribute to errors in the measurement of the lift-dependent drag characteristics. The introduction of $\Delta\alpha_{\text{flow}}$ provides only an average correction and does not correct for the changes in the spanwise load distribution as a result of possible angularity variations across the test section. Thus, minimal and constant flow angularity at the wing location in the test section is required to determine accurately the lift-dependent drag.

More detailed experiments, including surface-pressure measurements, are necessary to further explore the lift and drag characteristics of wings with highly swept tips such as the crescent wing.

Appendix A: Error Analysis

The uncertainties in the data are the result of measurement inaccuracies in the balance normal force F_N , the balance axial force F_A , the angle of attack α , and the dynamic pressure q . Consequently, the maximum errors in the normal-force coefficient C_N and the axial-force coefficient C_A are the following (neglecting terms of second and higher order):

$$|\Delta C_N| = \left(\frac{|\Delta F_N|}{F_N} + \frac{|\Delta q|}{q} \right) C_N \quad (\text{A1})$$

$$|\Delta C_A| = \left(\frac{|\Delta F_A|}{F_A} + \frac{|\Delta q|}{q} \right) C_A \quad (\text{A2})$$

where the Δ values represent the measurement errors. The lift and drag coefficients are derived from C_N , C_A , and α as follows:

$$C_L = C_N \cos \alpha - C_A \sin \alpha \quad (\text{A3})$$

$$C_D = C_A \cos \alpha + C_N \sin \alpha \quad (\text{A4})$$

From Eq. (A3), and neglecting terms of second order and higher, we obtain the maximum error in C_L :

$$|\Delta C_L| = |\Delta C_N| + \alpha |C_A| + C_A |\Delta \alpha| \quad (\text{A5})$$

where $\Delta\alpha$ represents the uncertainty in the α measurement. In the same manner, the following expression for the maximum error in C_D can be obtained from Eq. (A4):

$$|\Delta C_D| = |\Delta C_A| + C_N |\Delta \alpha| + \alpha |\Delta C_N| \quad (\text{A6})$$

Equation (A6) demonstrates the significant effect of errors in the angle-of-attack measurement on the accuracy of the drag coefficient. For negligible ΔC_A and ΔC_N , a relatively small error $|\Delta \alpha| = 0.1$ deg will result in an error in the drag coefficient $|\Delta C_D| = 17$ counts at a lift coefficient $C_L \cong C_N = 1.0$.

This will produce an error in the Oswald efficiency factor $|\Delta e| = 0.029$ for an aspect ratio 7 wing with $e = 0.9$. Note the uncertainty in the α measurement was ± 0.025 deg for the experiment reported herein.

Acknowledgments

The work of the first author was supported under NASA Langley Grant NAG 1-732 and NASA Ames Joint Research Interchange NCA2-397. The second author's work was supported under NASA Langley Contract NAS1-18240. The authors would like to acknowledge the assistance of the personnel of the 14×22 ft subsonic tunnel of the NASA Langley Research Center.

References

- ¹Van Dam, C. P., "Induced-Drag Characteristics of Crescent-Moon-Shaped Wings," *Journal of Aircraft*, Vol. 24, No. 2, 1987, pp. 115-119.
- ²Burkett, C. W., "Reduction in Induced Drag by the Use of Aft Swept Wing Tips," *Aeronautical Journal*, Vol. 93, Dec. 1989, pp. 400-405.
- ³Prandtl, L., "Application of Modern Hydrodynamics to Aeronautics," NACA TR116, 1921.
- ⁴Munk, M. M., "The Minimum Induced Drag of Aerofoils," NACA TR121, 1921.
- ⁵Vijgen, P. M. H. W., van Dam, C. P., and Holmes, B. J., "Sheared Wing-Tip Aerodynamics: Wind-Tunnel and Computational Investigation," *Journal of Aircraft*, Vol. 26, No. 3, 1989, pp. 207-213.
- ⁶Holbrook, G. T., Morris Dunham, D., and Greene, G. C., "Vortex Wake Alleviation Studies with a Variable Twist Wing," NASA TP2442, Nov. 1985.
- ⁷Van Dam, C. P., Vijgen, P. M. H. W., and Holmes, B. J., "Aerodynamic Characteristics of Crescent and Elliptic Wings at High Angles of Attack," *Journal of Aircraft*, Vol. 28, No. 4, 1991, pp. 253-260.
- ⁸Jacobs, E. N., and Ward, K. E., "Interference of Wing and Fuselage from Tests of 209 Combinations in the N.A.C.A. Variable-Density Tunnel," NACA TR540, 1935.
- ⁹Braslow, A. L., and Knox, E. C., "Simplified Method for Determination of Critical Height of Distributed Roughness Particles for Boundary-Layer Transition at Mach Numbers from 0. to 5.," NACA TN-4363, Sept. 1958.
- ¹⁰Poll, D. I. A., "Transition in the Infinite Swept Attachment-Line Boundary Layer," *The Aeronautical Quarterly*, Vol. 30, Pt. 4, Nov. 1979, pp. 607-629.
- ¹¹Rae, W. H., Jr., and Pope, A., *Low-Speed Wind Tunnel Testing*, 2nd ed., Wiley, New York, 1984.
- ¹²Maskew, B., "Prediction of Subsonic Aerodynamic Characteristics—A Case of Low-Order Panel Methods," *Journal of Aircraft*, Vol. 19, No. 2, 1982, pp. 157-163.
- ¹³Eppler, R., and Somers, D. M., "A Computer Program for the Design and Analysis of Low-Speed Airfoils," NASA TM-80210, March 1980.
- ¹⁴Schlichting, H., and Truckenbrodt, E., *Aerodynamics of the Airplane*, McGraw-Hill, New York, 1979.